



# Evaluation of structural and multifunctional properties of BaTiO<sub>3</sub>–NiFe<sub>2–x</sub>Sm<sub>x</sub>O<sub>4</sub> ceramic composites

Mehjabeen Khan<sup>1</sup> · Jyoti Shukla<sup>1</sup> · Pallavi Saxena<sup>1</sup> · Ashutosh Mishra<sup>1</sup> · Pradeep Sharma<sup>2</sup>

Received: 23 August 2022 / Accepted: 9 November 2022 / Published online: 29 November 2022  
© The Author(s), under exclusive licence to Springer-Verlag GmbH, DE part of Springer Nature 2022

## Abstract

In this paper, the multi-phase ceramic composites, consisting of dielectric barium titanate BaTiO<sub>3</sub> (BTO) and rare-earth-doped magnetic spinel ferrite NiFe<sub>2–x</sub>Sm<sub>x</sub>O<sub>4</sub> (NFSO) with  $x=0.00, 0.10, \text{ and } 0.20$  were synthesized through solid-state route. The structure of the prepared samples has been examined through XRD. The results indicate the occurrence of both perovskite (BaTiO<sub>3</sub>) and spinel (NiFe<sub>2–x</sub>Sm<sub>x</sub>O<sub>4</sub>) phases in the prepared composites. The magnetic as well as dielectric properties of the prepared samples were investigated and P–E hysteresis loops were recorded at various voltages. It has been found that the higher Sm concentration composite exhibits high dielectric permittivity (~9200) along with high remnant polarization (0.54  $\mu\text{C}/\text{cm}^2$ ) and low saturation magnetization (12 emu/g) at room temperature. The analysis showed that the ferrite phase (NFSO) has influenced the magnetic properties and dielectric response of BaTiO<sub>3</sub> material.

**Keywords** Ferrites · Sol–gel auto combustion · XRD · Dielectric behavior · Composites

## 1 Introduction

Research in material science is currently concentrated on multifunctional materials with several physical characteristics that can be modified at the same time [1]. Multiferroic materials are one of the most common types, which simultaneously exhibit one or more ferroic order parameters (a charge, spin, or/strain phenomena), notably ferromagnetism, ferroelectricity, and ferroelasticity, in the same phase. Additionally, these materials contain a variety of fascinating aspects, such as magnetism, which can be utilized for multifunctional applications [2].

Multiferroic materials are of two types: single-phase and multi-phase composites. In single-phase, both ferroic orders occur inside the same phase. The natural occurrence of multiferroism in materials is extremely scarce, as the mutual presence of ferroelectric and ferromagnetic properties in a single compound is a basic requirement [3]. Several materials, including YMnO<sub>3</sub>, TbMnO<sub>3</sub>, BiMnO<sub>3</sub>, and BiFeO<sub>3</sub>,

have been extensively explored due to the significance of this type of material and were discovered to possess intriguing characteristics. In BiFeO<sub>3</sub>, the Bi<sup>3+</sup> lone pair (A-site) is the primary source of polarization, whereas the Fe<sup>3+</sup> is the primary source of magnetization (B-site). A, B, or A/B-site doping can significantly influence the material's ferroelectric and magnetic properties. Above room temperature, the applicability of BiFeO<sub>3</sub> for multiferroic devices has been restricted because of its poor resistivity and uneven spin symmetry (*weak magnetic features*) [4].

The research on the bismuth ferrite system reveals some inherent problems, such as high leakage current density and structural instability, which have a significant impact on the material's capacitive, resistive, and ferroelectric properties [5, 6]. To address the leakage current density and related issues, innovative ways have been explored to build artificial multiferroic materials such as multi-phase or multiferroic composites. The peculiarity of these composites is that they have more design freedom, ME coupling is a few orders of magnitude higher than single-phase multiferroics, and can function at and above room temperature. Multiphase multiferroics composite design provides a unique platform for multifunctional devices such as spintronics, sensors, transducers, and terahertz radiation among others [7]. To improve magneto-electric (ME) coupling in a multiferroic composite, the ferroelectric phase should have a high dielectric constant

✉ Mehjabeen Khan  
mehjabeen.khan2013@gmail.com

<sup>1</sup> School of Physics, Devi Ahilya University, Khandwa Road Campus, Indore 452001, India

<sup>2</sup> Govt. Holkar Science College, Indore 452001, India

and low dielectric loss, while the ferrite phase should have a high magnetostriction value.

Multiferroic composites based on titanates and spinel ferrites are the subject of a lot of studies. Vast research on  $\text{BaTiO}_3\text{-NiFe}_2\text{O}_4$  multiferroic composites (MFC) with a variety of dopants has been carried out till now, wherein the dielectric, magnetic, and magneto-dielectric characteristics are thoroughly investigated [8–11]. The most commonly investigated MFC systems for research are  $(x)\text{BaTiO}_3 + (1-x)\text{Ni}_{0.93}\text{Cu}_{0.02}\text{Co}_{0.05}\text{Fe}_2\text{O}_4$  [12]. The dielectric constant increases as the ferroelectric concentration increases, but the Curie temperature drops. The magneto-electric effect and dielectric behavior of  $(x)\text{Ni}_{0.93}\text{Co}_{0.02}\text{Mn}_{0.05}\text{Fe}_{1.95}\text{O}_4 + (1-x)\text{Na}_{0.5}\text{Bi}_{0.5}\text{TiO}_3$  and  $\text{Ni}_{0.75}\text{Zn}_{0.25}\text{Fe}_2\text{O}_4\text{-BaTi}_{0.85}\text{Zr}_{0.15}\text{O}_3$  [13, 14] were examined using a solid-state reaction technique. The dielectric constant was found to decrease with increasing frequency. At lower frequencies, this decline is found to be rapid and sluggish at higher frequencies. However, there has been no improvement in the coupling effect between the barium titanate and spinel nickel ferrite phases. A unique technique is employed to improve the ME coupling by increasing the dielectric constant of the BT phase and the magnetostriction of the magnetic phase, which may be accomplished by doping these ferroic phases with rare-earth ions.

Rare earth ions are one of the highly promising alternatives to enhance the features of spinel ferrites. Due to its fascinating magnetic moment and larger ionic radii, the samarium is an ideal choice for improving the dielectric and magnetic characteristics of  $\text{NiFe}_2\text{O}_4$ . The partial replacement of  $\text{Fe}^{3+}$  (0.645 Å) ion by  $\text{Sm}^{3+}$  ions with a larger ionic radius (0.958 Å) induces structural distortion, which induces strain and thus drastically changes the dielectric properties. The ionic radii of the corresponding elements are taken from Shannon's ionic radii database according to the six-fold coordination of oxygen ions [15]. Samarium doping in the nickel ferrite phases increases the dielectric constant, increases polarization, and reduces dielectric loss, as previously reported [16].

Keeping these points in mind, we substituted the samarium ( $\text{Sm}^{3+}$ ) ion into the nickel ferrite phase and combined it with the ferroelectric phase of  $\text{BaTiO}_3$ . The solid-state reaction and sol-gel auto-combustion approaches have been used to make the composites [17, 18]. We have used the solid-state reaction approach to synthesis the  $0.67\text{BaTiO}_3\text{-}0.33\text{NiFe}_{(2-x)}\text{Sm}_{(x)}\text{O}_4$  composite ceramics ( $x = 0.00, 0.10, \text{ and } 0.20$ ). This approach was chosen for the reason that it produces dense microstructures, which is an essential step in improving the interaction between grains of two ferroic phases in composites. To the best of our knowledge, no studies have been conducted on multiferroicity in particulate  $0.67\text{BaTiO}_3\text{-}0.33\text{NiFe}_{(2-x)}\text{Sm}_{(x)}\text{O}_4$  multiferroic composites. The ratio  $0.67\text{BaTiO}_3\text{-}0.33\text{NiFe}_{(2-x)}\text{Sm}_{(x)}\text{O}_4$  has

been purposely selected to avoid the suppression of the ferroelectric (BTO) phase. This study aims to go through the structural, dielectric, ferroelectric, and magnetic characteristics of the prepared composites and to bring out valuable insight from them for future reference.

## 2 Experimental details

### 2.1 Sample preparation

#### 2.1.1 Materials required

The individual phases of  $\text{NiFe}_{2-x}\text{Sm}_x\text{O}_4$  (where  $x = 0.00, 0.10, \text{ and } 0.20$ ) and  $\text{BaTiO}_3$  were prepared by the sol-gel auto-combustion method. For this goal, highly pure raw chemical materials from Sigma Aldrich, *i.e.*, iron(III) nitrate nonahydrate purified  $\text{Fe}(\text{NO}_3)_3 \cdot 9\text{H}_2\text{O}$  [ $\geq 98\%$ ], nickel(II) nitrate AR hexahydrate  $\text{Ni}(\text{NO}_3)_2 \cdot 6\text{H}_2\text{O}$  [ $99\%$ ], nitric acid  $\text{HNO}_3$ , samarium nitrate (*prepared by  $\text{Sm}_2\text{O}_3$  [ $99\%$ ] and nitric acid*), barium(II) nitrate ( $\text{Ba}(\text{NO}_3)_2$ ) [ $\geq 98\%$ ], titanyl oxynitrate ( $\text{TiO}(\text{NO}_3)_2$ ) (*prepared by  $\text{Ti}(\text{C}_4\text{H}_9\text{O})_4$  [ $99\%$ ] and nitric acid  $\text{HNO}_3$* ), citric acid anhydrous  $\text{C}_6\text{H}_8\text{O}_7$ , ethylene glycol  $\text{C}_2\text{H}_6\text{O}_2$ , ammonia solution  $\text{NH}_4\text{OH}$ , polyvinyl alcohol ( $\text{C}_2\text{H}_4\text{O}$ )<sub>*n*</sub>, and distilled water were selected. The required ratio of metal nitrates was liquefied individually in a minimum amount of distilled water and then mixed with an aqueous solution of citric acid. The obtained solution was further stirred on a magnetic stirrer until a homogenous mixture was obtained. The ammonia solution ( $\text{NH}_4\text{OH}$ ) was introduced into the homogenous mixture to adjust the pH value of 7. The well-stirred homogenous neutralized solution was heated and stirred at the temperature of about  $90^\circ\text{C}$  until it is converted into the form of viscous gel, which was further heated at  $400^\circ\text{C}$  on heating calotte to achieve a self-propagation reaction. The as-prepared powder was thermally treated at  $900^\circ\text{C}$  for 2 h for phase formation [16, 19].

#### 2.1.2 Synthesis of $0.67\text{BaTiO}_3\text{-}0.33\text{NiFe}_{2-x}\text{Sm}_x\text{O}_4$ composites

For the synthesis of  $0.67\text{BaTiO}_3\text{-}0.33\text{NiFe}_{2-x}\text{Sm}_x\text{O}_4$  composites, the conventional solid-state reaction method has been used. Both these compounds  $\text{BaTiO}_3$  (BT) and  $\text{NiFe}_{2-x}\text{Sm}_x\text{O}_4$  (NFS0) were taken in appropriate proportion (2:1 wt ratio) to form  $0.67\text{BaTiO}_3\text{-}0.33\text{NiFe}_{2-x}\text{Sm}_x\text{O}_4$  (*abbreviated as BT-NFS0, BT-NFS1 and BT-NFS2 for  $x = 0.00, 0.10, 0.20$ , respectively*) composites, and ground using an agate mortar and pestle with acetone as a liquid medium. The obtained powders were compacted into disc-shaped pellets using a hydraulic press. All the pellets were sintered at  $1100^\circ\text{C}$  for 1 hour 20 min using a muffle furnace where the heating rate was  $5^\circ/\text{min}$  [20, 21].

## 2.2 Sample characterizations

To classify the phase formation and atomic arrangements of the sintered pellets, X-ray diffraction was recorded using the Bruker D8 advance equipped with a monochromatic CuK $\alpha$  source of radiation ( $\lambda = 1.5406 \text{ \AA}$ ). The scan speed was  $0.019^\circ/\text{s}$  and the scan angle ranged from  $10^\circ$  to  $90^\circ$ . To know the phase fraction of the sintered samples, Rietveld refinement was done using the Fullprof software. The FTIR measurement of the samples was done through the Perkin Elmer spectrophotometer over the wavenumber range  $1000\text{--}400 \text{ cm}^{-1}$  with  $0.5 \text{ cm}^{-1}$  transmission geometry. The room temperature dielectric measurement and complex impedance analysis were measured using the Broadband Dielectric Impedance analyzer (NovoControl) in the frequency range from 1 to  $10^6 \text{ Hz}$ . The radiant-precision material analyzer was used for the ferroelectric study at room temperature with each sample pressed and covered by silver electrodes on both sides. The room temperature PE measurement was performed using the RT66A Radiant ferroelectric loop tracer. The magnetic measurement of the prepared samples was carried out using a 14T PPMS vibrating sample magnetometer under the applied magnetic field of 20kOe.

## 3 Results and discussion

### 3.1 Structural study

The crystal structure and phase purity of BT-NFS0, BT-NFS1, and BT-NFS2 composites were investigated using the XRD technique, recorded in the range  $20^\circ\text{--}70^\circ$  which are displayed in Fig. 1. This demonstrates the presence of both the perovskite BT and spinel NFS phases in a variety of composites. Apart from these two phases, there is no evidence of any additional crystalline phase that could

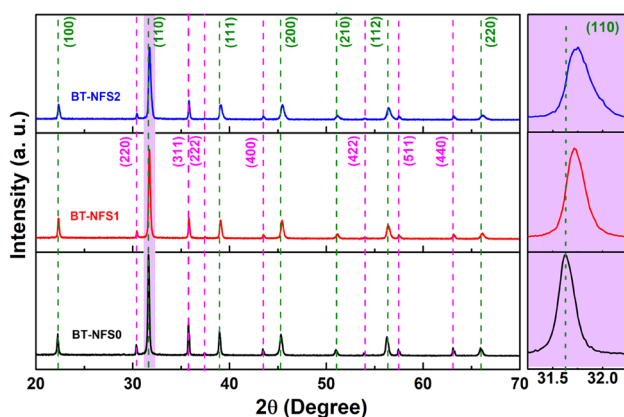


**Fig. 1** X-ray diffraction patterns of  $0.67\text{BaTiO}_3\text{--}0.33\text{NiFe}_{2-x}\text{Sm}_x\text{O}_4$  composites

be detected within the limits of the X-ray diffractometer. The peaks of BT diffraction indicate a tetragonal (JCPDS 89-1428, space group  $P4mm$ ) perovskite crystal system. Similarly, NFS0, NFS1, and NFS2 diffraction peaks corroborate the cubic (JCPDS 10-0325, space group  $Fd\text{-}3m$ ) inverse spinel structure [20, 22].

The Rietveld refinement study of BT-NFS0, BT-NFS1, and BT-NFS2 composites sintered at  $1100^\circ\text{C}$  is depicted in Fig. 2. The refined XRD profile was obtained using the Fullprof software and analyzed by providing the required structural information from the literature. It implies that the diffraction peaks in the BT phase belong to a tetragonal perovskite structure with a cubic spinel structure of NFS. The successful production of a dual-phase composite for each composition was validated by the absence of any undesirable phase. The consistency of the match to the observed XRD pattern was assessed using the Rietveld agreement factors ( $R_p$ ,  $R_{wp}$ , and  $\chi^2$ ). The Rietveld analysis revealed a high degree of similarity between the observed and calculated diffraction patterns (Fig. 2), which was validated by observing the patterns of difference in the measured and calculated XRD patterns. The refined structural parameters for both phases of the composites are shown in Table 1, which includes crystallite size, lattice parameter, and unit cell volume. The Rietveld refinement method is also used to determine phase fraction, as seen in Table 1. When the  $\text{Sm}^{3+}$  content is increased, the phase fraction of the BT phase increases while the ferrite phase falls. It implies that the  $\text{Sm}^{3+}$  did not form a solid solution or had very low solid solubility in spinel ferrites. Because the ionic radius of the  $\text{Sm}^{3+}$  ion is ( $0.958 \text{ \AA}$ ) greater than that of the  $\text{Fe}^{3+}$  ion ( $0.645 \text{ \AA}$ ), there is a solubility limit when  $\text{Fe}^{3+}$  ions are replaced by  $\text{Sm}^{3+}$  ions, and it may be assumed that these extra  $\text{Sm}^{3+}$  ions have accumulated inside the barium titanate due to higher

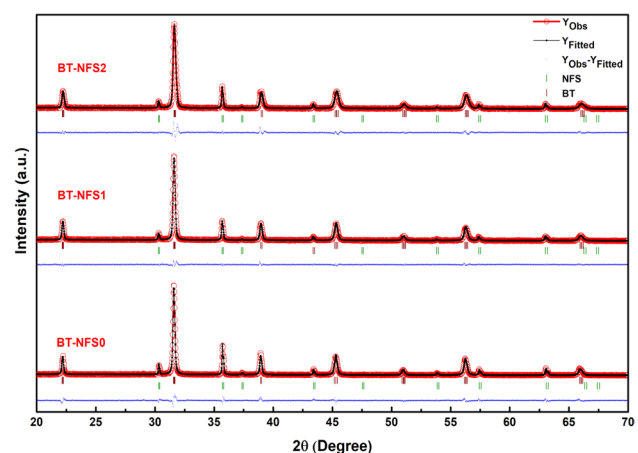


**Fig. 2** Rietveld's refinement of  $0.67\text{BaTiO}_3\text{--}0.33\text{NiFe}_{2-x}\text{Sm}_x\text{O}_4$  composites

**Table 1** Structural parameters of  $0.67\text{BaTiO}_3\text{-}0.33\text{NiFe}_2\text{O}_4$  using Reitveld refinement of XRD data

Parameters	X=0.00		X=0.10		X=0.20	
	BT	NFS0	BT	NFS1	BT	NFS2
Phase						
$2\theta$ range (deg.)	20–70	20–70	20–70	20–70	20–70	20–70
Step size	0.019	0.019	0.019	0.019	0.019	0.019
Wavelength	1.5405	1.5405	1.5405	1.5405	1.5405	1.5405
Space group	P4mm	Fd-3m	P4mm	Fd-3m	P4mm	Fd-3m
<i>a</i>	4.0007	8.3312	3.9986	8.3385	3.9941	8.3380
<i>b</i>	4.0007	8.3312	3.9986	8.3385	3.9941	8.3380
<i>c</i>	4.0115	8.3312	4.0097	8.3385	4.0071	8.3380
<i>c/a</i>	1.0026	1	1.0027	1	1.0032	1
Volume	64.204	578.264	64.110	579.778	63.925	579.680
Density (in gm/cm <sup>3</sup> )	6.038	5.236	6.068	5.418	6.243	5.788
Phase fraction	66.09	33.91	69.71	30.29	77.76	22.24
Crystallite size (in nm)	45.819	82.203	35.728	69.796	27.276	72.227
$R_f$	3.846	7.969	4.580	5.165	2.619	4.513
$R_{\text{brag}}$	4.605	9.178	3.013	3.129	4.556	5.365
$R_{\text{WP}}$	22.5		21.9		24.4	
$R_{\text{exp}}$	18.35		19.50		19.60	
$R_p$	25.9		23.4		25.9	
Zero point	0.0354		0.1189		0.1189	
GOF	1.2		1.1		1.2	
$\chi^2$	1.50		1.26		1.55	

ionic radius of  $\text{Ba}^{2+}$  (1.49 Å) [23, 24]. As a result, the phase fraction of the BT phase increases with  $\text{Sm}^{3+}$  content.

The diffraction peaks of BT-NFS1 and BT-NFS2 shifted toward a higher diffraction angle due to the substitution of rare-earth  $\text{Sm}^{3+}$  ion in BT-NFS0 composites, which is further demonstrated by the enlargement of the (110) highest peak in Fig. 1. The shifted diffraction peaks strongly confirm the incorporation of  $\text{Sm}^{3+}$  ion in BT-NFS0 composite; therefore, it indicates the lattice constant of the composite materials decreases with increasing  $\text{Sm}^{3+}$  concentration which can be seen in Table 1. In the BT phase, due to the larger ionic radius of  $\text{Ba}^{2+}$  as compared to  $\text{Sm}^{3+}$ , the value of the lattice parameters decreases with an increase in  $\text{Sm}^{3+}$  content [25]. On the other hand, in the NFS phase, the lattice parameter increases at first and subsequently drops. When Sm is doped in BT-NFS0 composites, the width of diffracted peaks of BT-NFS0 composite increases, as a result, the crystallite size of BT-NFS1 and BT-NFS2 decreases abruptly. This could be due to the difference of ionic radius between  $\text{Sm}^{3+}$ ,  $\text{Fe}^{3+}$ , and  $\text{Ba}^{2+}$  ions.

### 3.2 Fourier transform infrared spectroscopy

FTIR spectroscopy was utilized to explore the role of functional groups in BT-NFS0 and BT-NFS1 composites. Figure 3 shows the FT-IR spectra of all the composites obtained in the 400–1500  $\text{cm}^{-1}$  range and the band positions are shown in Table 2. The main absorption spectra

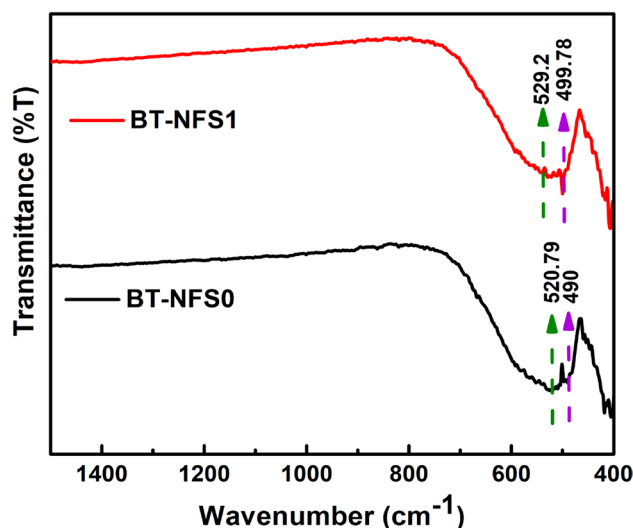


**Fig. 3** FTIR spectra of  $0.67\text{BaTiO}_3\text{-}0.33\text{NiFe}_{2-x}\text{Sm}_x\text{O}_4$  composites

are detected within 1000  $\text{cm}^{-1}$ . The two absorption bands about 520 and 405  $\text{cm}^{-1}$  correspond to the NF phase. The absorption band at 520  $\text{cm}^{-1}$  is caused by intrinsic stretching vibrations of metal-oxygen (M–O) bonds at tetrahedral locations and the second band, seen at about 405  $\text{cm}^{-1}$ , is caused by intrinsic stretching vibrations of M–O vibrations at octahedral sites [26, 27]. Both the composites revealed an absorption band at about 490  $\text{cm}^{-1}$

**Table 2** Absorption bands of 0.67BaTiO<sub>3</sub>-0.33NiFe<sub>2-x</sub>Sm<sub>x</sub>O<sub>4</sub> composites

Peak number	Sm-00		Sm-20	
	Wavenumber (cm <sup>-1</sup> )	Transmittance (%)	Wave-number (cm <sup>-1</sup> )	Transmittance (%)
1	520.09	67.91	539.15	70.87
2	490	69.58	529.2	69.97
3	459.33	78.48	510.3	70.22
4	418	63.47	499.78	66.57
5	405.35	62.56	-	-

that is associated with Ti-O octahedra stretching vibration [5]. The vibrations (stretching and bending) of the TiO<sub>6</sub> octahedron at the Ti-site of the BT phase create this large absorption band. Another characteristic band with very small intensity is observed around 1450 cm<sup>-1</sup> for both composites, which is mostly attributed to the signals of the Ba-Ti-O vibration [28, 29]. As a result, FTIR research confirms the appropriate phase identification of the composite material inferred previously from XRD analysis.

### 3.3 Electrical properties

#### 3.3.1 Dielectric constant

The dielectric constants such as relative permittivity (the real  $\epsilon'$  and the imaginary parts  $\epsilon''$ ) of BT-NFS0, BT-NFS1, and BT-NFS2 composites have been determined at room temperature, in the frequency range 1–10<sup>6</sup> Hz and are presented in Fig. 4a and c. The real component ( $\epsilon'$ ) denotes the stored energy per cycle along with polarizations, while the imaginary part ( $\epsilon''$ ) denotes the energy loss per cycle owing to the heat, conductivity, and charge leakage. Figure 4 depicts two types of fluctuations in dielectric permittivity, one as a function of frequency and the other as a function of Sm<sup>3+</sup> ion composition. Both the components of dielectric constants ( $\epsilon'$  and  $\epsilon''$ ) drop with increasing frequency. This drop is found to be faster at lower frequencies and becomes nearly constant at higher frequencies. At lower frequencies, molecular polarization can be aligned and oscillate under the influence of an external field, resulting in a high dielectric constant. As the frequency increases, the dipole oscillation can no longer follow the external frequency, causing the polarization response to drop and become nearly constant. In general, a drop in the dielectric constant is caused by the long relaxation time of the polarization with frequency

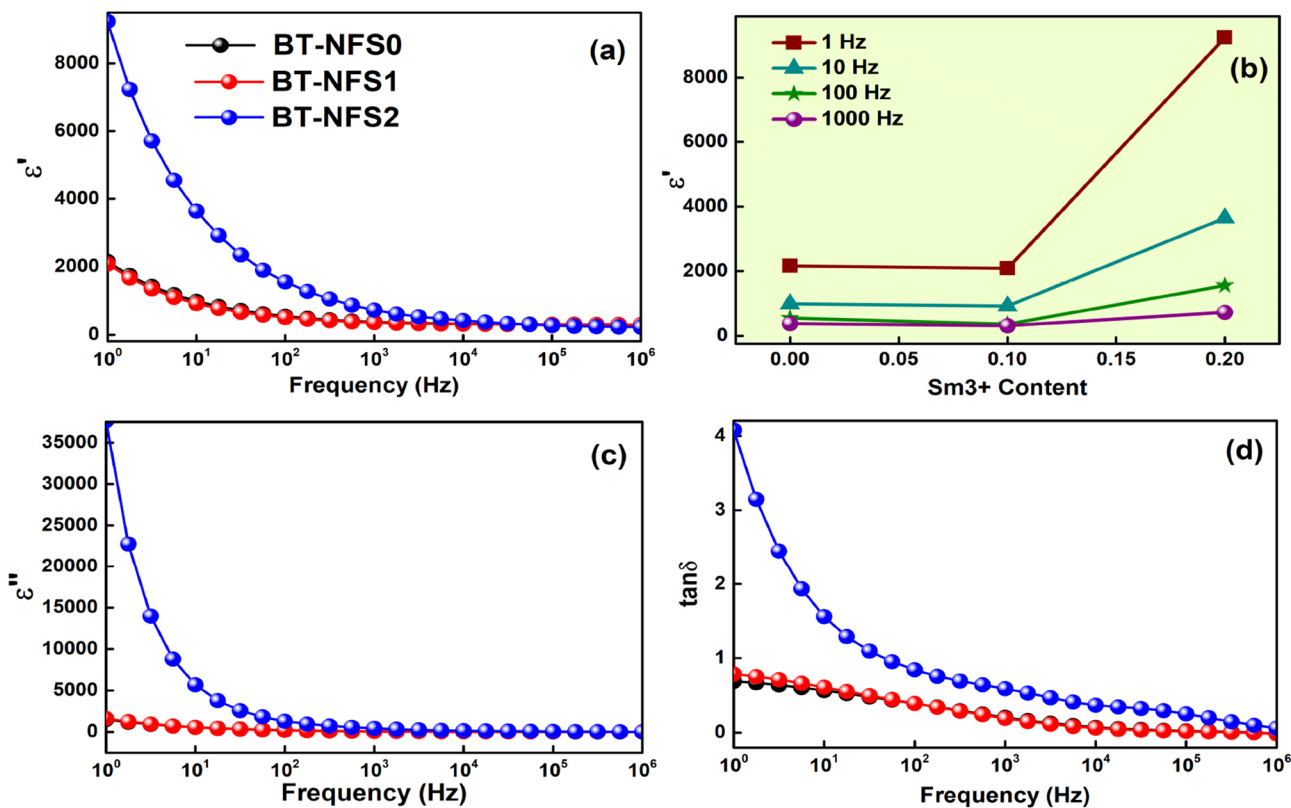


**Fig. 4** Variation of dielectric constant and dielectric loss against frequency for 0.67BaTiO<sub>3</sub>-0.33NiFe<sub>2-x</sub>Sm<sub>x</sub>O<sub>4</sub> composites

[30, 31]. In these composites, the orientation and space charge polarizations have a larger role. The contribution of surface charge polarization to dielectric response can also be described using the Maxwell–Wagner interfacial model [32]. According to this model, these materials are made up of well-conducting grains separated by a thin layer of poor-conducting grains. The grain having good conductivity dominates at a higher frequency while grain boundaries with poor conductivity are effective at lower frequencies [16]. Furthermore, the behavior of the dielectric constant as a function of  $\text{Sm}^{3+}$  ion content in BT-NFS0 composites has been investigated. The permittivity ( $\epsilon'$ ) values at 1 Hz for all  $\text{Sm}^{3+}$ -doped BT-NFS0 composites are presented in Table 3. Initially dielectric constant ( $\epsilon''$ ) of BT-NFS0 and BT-NFS1 is nearly constant at lower concentrations of  $\text{Sm}^{3+}$ . The dielectric constant ( $\epsilon'$ ) of the BT-NFS2 composite is much higher as compared to other composites. This could be owing to  $\text{Sm}^{3+}$  ions having a larger ionic radius than  $\text{Fe}^{3+}$  ions. So, there is a solubility limit for  $\text{Sm}^{3+}$  ions substitution, and it may be assumed that these extra  $\text{Sm}^{3+}$  ions have accumulated inside the BT phase due to the higher ionic radius of  $\text{Ba}^{2+}$  (1.49 Å). As a result, the phase fraction of BT increases with  $\text{Sm}^{3+}$  content. Because of the extremely ferroelectric nature of the BT phase, the dielectric constant rises. The  $c/a$  ratios for BT-NFS0, BT-NFS1, and BT-NFS2 are 1.0026, 1.0027, and 1.0032, respectively, which are shown in Table 1 (XRD results). The rising value of  $c/a$  could also explain the improvement in  $\epsilon'$ . Furthermore, the dielectric behavior of composites can be influenced by two factors space charge polarization and grain size distribution. The space charge polarization may have resulted as a consequence of the charge compensation due to extra  $\text{Sm}^{3+}$  ions accumulated on  $\text{Ba}^{2+}$  [25].

### 3.3.2 Dielectric loss

Dielectric loss or loss tangent ( $\tan \delta$ ) is another important property that has been studied for current magneto-dielectric composite systems, which was derived by dividing the imaginary part of the complex permittivity by the real part. Dielectric loss is the amount of energy lost as heat as a

result of grain boundary, impurity, crystal defect, and structural inhomogeneities [33]. The fluctuation of the dielectric loss as a function of frequency is depicted in Fig. 4d. As the frequency rises, the dielectric loss decreases. The loss was found to be extreme at lower frequencies and it drops at higher frequencies. A step kind of behavior has been observed at around 3 kHz for all the samples. The electron hopping between the  $\text{Fe}^{2+}$  and  $\text{Fe}^{3+}$  sites is responsible for this [34]. The loss values at 1 Hz are given in Table 3. It has been perceived that dielectric loss increases with  $\text{Sm}^{3+}$  concentration in BT-NFS0 composites, since extra  $\text{Sm}^{3+}$  ions have accumulated inside the BT phase due to the higher ionic radius of  $\text{Ba}^{2+}$  (1.49 Å). When the content of a dopant ion ( $\text{Sm}^{3+}$ ) is increased with a different ionic state of the host cation ( $\text{Ba}^{2+}$ ), two processes occur: the first is the development of defects or vacancies, and the second is a change in carrier concentration inside the dipole area [35]. Both of these scenarios might cause enhancement in the dielectric constant and loss value. As a consequence, it is apparent that  $\text{Sm}^{3+}$  doping generates defects and voids in the composite material by increasing carrier concentration.

### 3.3.3 AC conductivity

To acquire a better knowledge of the electrical conduction mechanism, the conductivity spectra of BT-NFS0, BT-NFS1, and BT-NFS2 composites have been carried out with a frequency range 1 Hz–1 MHz. The separation of the spectra into two halves is depicted in Fig. 5. The conductivity of composites in the first half spectra (region-I) does not respond to the applied frequency and is almost constant at lower frequencies ( $1-10^3$  Hz). The value of constant conductivity is known as dc conductivity, and this region is known as the plateau region. This plateau region corresponds to the movement of the charge carriers across the insulating grain boundary. In the second half spectra (region-II), the conductivity rises dramatically in frequency. This region-II ( $10^4-10^6$  Hz) is known as the dispersion region, and it corresponds to grain conduction or increased charge carrier mobility. Additionally, a strong conduction mechanism between the  $\text{Fe}^{3+}/\text{Fe}^{2+}$  and  $\text{Ti}^{4+}/\text{Ti}^{3+}$  ions could be created at

**Table 3** Dielectric constant and loss tangent, polarization, and coercivity of  $0.67\text{BaTiO}_3-0.33\text{NiFe}_{2-x}\text{Sm}_x\text{O}_4$  composites

Sample	Dielectric constant	Dielectric constant	Dielectric loss	$+P_r$ ( $\mu\text{C}/\text{cm}^2$ )	$P_{\text{max}}$ ( $\mu\text{C}/\text{cm}^2$ )	Coercivity (Kv/cm)	Loop area ( $\mu\text{C}/\text{cm}^2$ )
Frequency	1 Hz	10 Hz	10 Hz	10 Hz	10 Hz	10 Hz	10 Hz
				(1000 V)	(1000 V)	(1000 V)	(1000 V)
BT-NFS0	2160	988	0.49	$1.93 \times 10^{-1}$	0.631	3.31	$5.24 \times 10^2$
BT-NFS1	2087	916	0.55	$3.42 \times 10^{-1}$	0.741	4.43	$9.21 \times 10^2$
BT-NFS2	9240	3646	1.56	$5.35 \times 10^{-1}$	0.953	5.62	$1.48 \times 10^3$

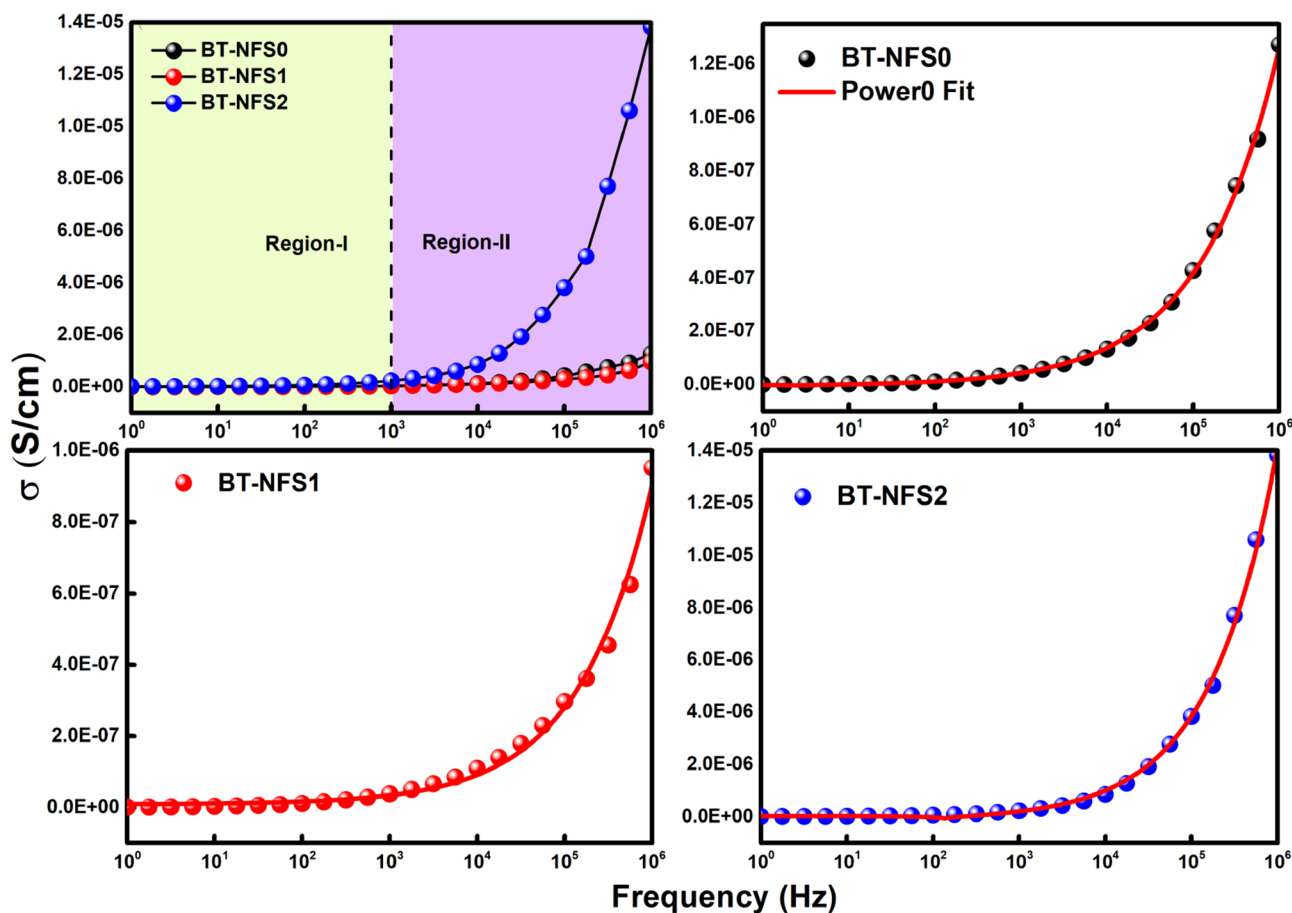


Fig. 5 Variation of ac conductivity as a function of frequency for 0.67BaTiO<sub>3</sub>-0.33NiFe<sub>2-x</sub>Sm<sub>x</sub>O<sub>4</sub> composites

Table 4 Fitted different parameters using the power law of Jonscher’s for 0.67BaTiO<sub>3</sub>-0.33NiFe<sub>2-x</sub>Sm<sub>x</sub>O<sub>4</sub> composites

Sample	$\sigma_{dc}$ (S/cm)	A (Polarizability strength)	S (Degree of correlation)	R <sup>2</sup>
BT-NFS0	$3.07623 \times 10^{-9}$	$1.75 \times 10^{-9}$	0.476	0.998
BT-NFS1	$9.17256 \times 10^{-9}$	$6.87 \times 10^{-10}$	0.519	0.992
BT-NFS2	$6.36476 \times 10^{-8}$	$6.26 \times 10^{-9}$	0.559	0.998

high frequencies [36, 37]. Ceramic conductivity is calculated using Jonscher's universal power law [38] in most materials and is shown in Table 4.

$$\sigma_{ac} = \sigma_{dc} + A\omega^n$$

where  $\sigma_{ac}$  stands for ac conductivity,  $\sigma_{dc}$  is the dc limit of the conductivity,  $A\omega^n$  is a term used to describe transport properties of the charging carriers (that could be polarons, ions, and electrons), 'A' stands for the pre-exponential component that defines the polarizability strength,

'n' stands for the fractional exponent (between 0 and 1) that offers information about the degree of correlation between ion hops during the conduction process. By analyzing the results, there is a plateau region for the conductivity spectrum for all the samples, which corresponds to the grain boundary (at a lower frequency) and the contribution of grain (at a higher frequency). The conductivity spectra that have been well equipped with Jonscher’s power law are shown in Fig. 5. With rising frequency, the AC conductivity values of all the samples were found to grow. This conductivity process in ferrites is responsible owing to the exchange of electrons between Fe<sup>2+</sup> and Fe<sup>3+</sup> and the presence of oxygen vacancies. If the frequency is raised, the conductive grains become more active in the sample. The electrons were then jumped in Fe<sup>2+</sup> and Fe<sup>3+</sup> ions. Therefore, the AC conductivity will also increase with rising frequency. Figure 5 also shows the compositional variability of rare-earth ion (Sm<sup>3+</sup>)-doped nickel ferrite conductivity spectra and found that NiFe<sub>2-x</sub>Sm<sub>x</sub>O<sub>4</sub> conductivity increases with an increase in Sm<sup>3+</sup> material. This is due to the small polaron hopping [13, 39].

### 3.4 Ferroelectric study

The ferroelectric characteristics of BT-NFS0, BT-NFS1, and BT-NFS2 are measured using polarization versus the electric field throughout a frequency range of 10 Hz. The P–E loops for BT-NFS0, BT-NFS1, and BT-NFS2 are compared in Fig. 6. The BT-NFS0 composite has a lower  $P_{\max}$  (maximum polarization) than the other two. All of the composites have unsaturated polarization, which represents poor ferroelectricity in these composites. The unsaturated P–E loops of all composites also signify that leakage current contributions are minimal [40]. The ferroelectric characteristics such as maximum polarization ( $P_{\max}$ ), remnant polarization ( $P_r$ ) and coercive field ( $E_c$ ) of all the composites are measured using P–E hysteresis loops, which are shown in Table 4. The ferroelectric characteristics of BT-NFS1 and BT-NFS2 composites are larger than those of BT-NFS0 composites.

As the concentration of Sm in BT-NFS0 increases, so does its  $P_{\max}$  values. Moreover, the values of  $P_r$  and  $E_c$  of BT-NFS0 composite also increase with the increased concentration of Sm in BT-NFS0 composite. An increase in coercivity ( $E_c$ ) indicates that the Sm-doped nickel ferrite

element in the ferroelectric matrix is pinning the motion of the ferroelectric domains [41]. The area of the loop also increases when  $\text{Sm}^{3+}$  is doped in BT-NFS0. The deviations in the ferroelectric behavior of the BT-NFS0 composite might be due to the grain size effect and oxygen vacancy [42].

### 3.5 Magnetic measurement

Computing magnetization versus magnetic field loops yields the magnetic characteristics of all composites. Figure 7 shows the magnetization of BT-NFS0, BT-NFS1, and BT-NFS2 composite ceramics under a magnetic field  $\pm 20$  kOe at room temperature. The inset of Fig. 7 shows a broad view of the M–H loop of the BT-NFS0, BT-NFS1, and BT-NFS2 composites, with fields ranging from  $-1$  kOe to  $1$  kOe. The magnetic characteristics such as saturation magnetization ( $M_s$ ), coercive field ( $H_c$ ), and remnant magnetization ( $M_r$ ) for all the composites are shown in Table 5. Comparisons between these magnetic parameters are shown in Fig. 8. The saturation magnetization ( $M_s$ ) of the BT-NFS0 composite decreases as the content

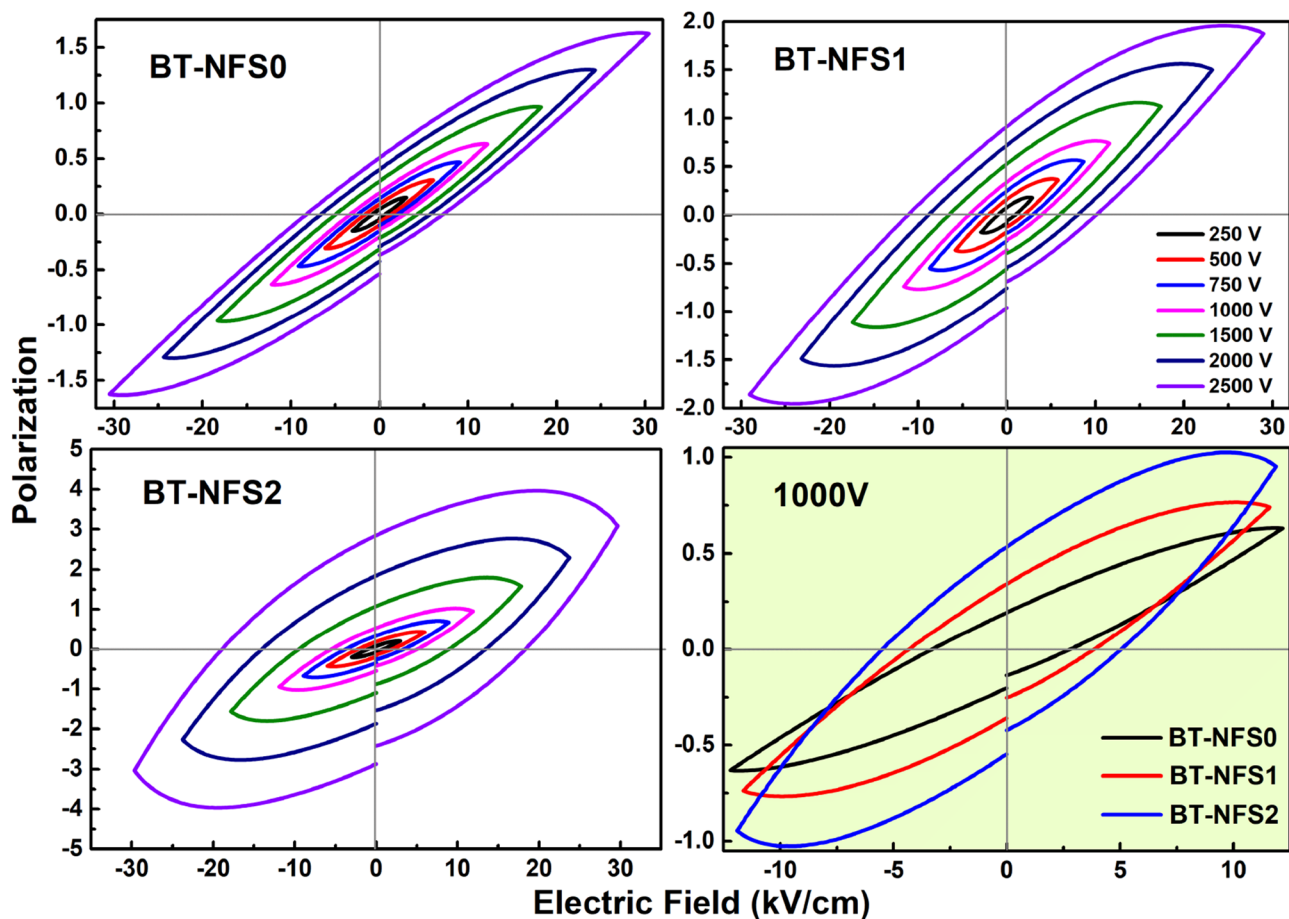
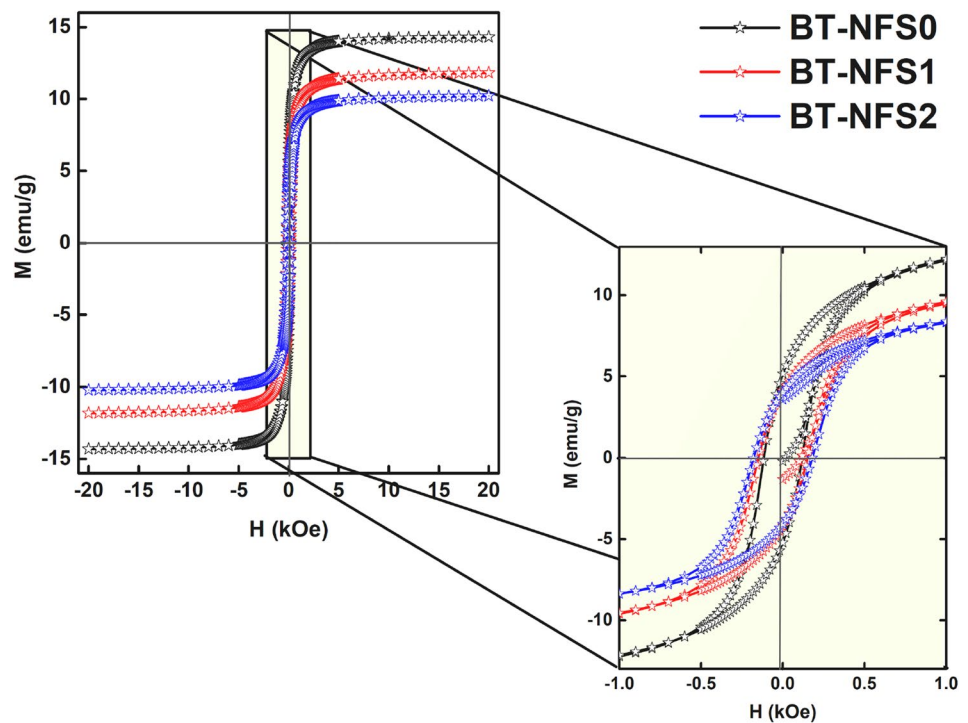


Fig. 6 PE hysteresis loops for  $0.67\text{BaTiO}_3-0.33\text{NiFe}_{2-x}\text{Sm}_x\text{O}_4$  composites



**Fig. 7** sM–H curves of 0.67BaTiO<sub>3</sub>-0.33NiFe<sub>2-x</sub>Sm<sub>x</sub>O<sub>4</sub> composites



**Table 5** Magnetic parameters of 0.67BaTiO<sub>3</sub>-0.33NiFe<sub>2-x</sub>Sm<sub>x</sub>O<sub>4</sub>

Sample name	<i>M<sub>s</sub></i> (emu/gram)	<i>M<sub>r</sub></i> (emu/gram)	<i>H<sub>c</sub></i> (Oe)	SQR ( <i>M<sub>r</sub></i> / <i>M<sub>s</sub></i> )	<i>μ<sub>B</sub></i> (B)
BT-NFS0	14.41	5.17	117.0	0.35	0.60
BT-NFS1	11.97	4.45	148.7	0.37	0.50
BT-NFS2	10.28	4.19	177.2	0.40	0.44

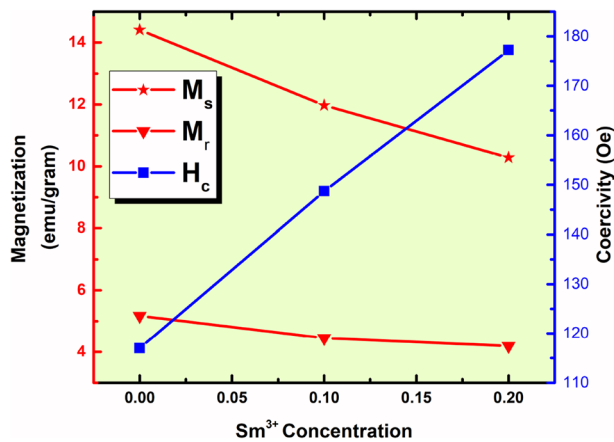


**Fig. 8** Comparison of M–H values for 0.67BaTiO<sub>3</sub>-0.33NiFe<sub>2-x</sub>Sm<sub>x</sub>O<sub>4</sub> composites

of Sm<sup>3+</sup> increases in these composites. The value of *M<sub>r</sub>* also drops as the concentration of Sm<sup>3+</sup> increases in the BT-NFS0 composite. This declining behavior in magnetic parameters could be due to a mismatch of ionic radii and magnetic moments of Sm<sup>3+</sup>, Fe<sup>3+</sup>, and Ba<sup>2+</sup> ions. The

mismatch of ionic radius creates lattice distortion [43, 44]. The magnetic moment of Sm<sup>3+</sup> is lower than Fe<sup>3+</sup>, while Ba<sup>2+</sup> is a non-magnetic ion. As a result, ferromagnetic behavior drops as the concentration of Sm<sup>3+</sup> ion increases. The value of the coercive magnetic field (*H<sub>c</sub>*) of BT-NFS0 increases when the Sm<sup>3+</sup> ion is substituted in these composites. This enhancement could be due to domain pinning, which puts a constraint on the domain wall motion of the magnetic NFS phase in composites and results in hysteresis loops with induced coercivity. The Bohr magnetons of the BT-NFS0, BT-NFS1, and BT-NFS2 composites are determined using the equations below [29].

$$\mu_B = \frac{M \times M_s}{5885}$$

where *μ<sub>B</sub>* stands for Bohr's magnetron, *M<sub>s</sub>* stands for saturation magnetization, *M* stands for molecule weight of composites, and 5885 is for magnetic factor. The values of Bohr's magnetron for all the composites are shown in Table 5. With an increase in the concentration of Sm<sup>3+</sup> in BT-NFS0, the magnetic moment of composites in terms of Bohr's magnetron (*B*) is reduced, which could be due

to the lower magnetic moment of  $\text{Sm}^{3+}$  ion as compared to the  $\text{Fe}^{3+}$  ions. Table 5 also shows how the squareness of BT-NFS0 composites varied with  $\text{Sm}^{3+}$  ions. Using the equations  $M_r/M_s$ , the squareness of BT-NFS0, BT-NFS1, and BT-NFS2 composites is calculated. The squareness of all composites is less than 0.5, indicating tiny domains formed by a randomly oriented assemblage of spherical particles, confirming the samples' anisotropic character. The area under the curve of BT-NFS0 composite drops as the concentration of Sm in it increases, indicating that all composites are soft magnetic.

## 4 Conclusion

The BT-NFS0, BT-NFS1, and BT-NFS2 particulate multi-ferroic composites have been successfully prepared through a solid-state reaction route. The XRD analysis of the prepared composites disclosed the presence of both the perovskite and spinel phase without any other impurity phase. With the increase in  $\text{Sm}^{3+}$  ion concentration in BT-NFS0, the phase fraction of the BT phase increases and the ferrite phase falls. The  $c/a$  ratio for BT-NFS0, BT-NFS1, and BT-NFS2 is increased with the increase in  $\text{Sm}^{3+}$  content. Due to the extremely high ferroelectric nature of the BT phase and the increase of the  $c/a$  ratio, the dielectric constant rises. The development of vacancies, defects, and the change in carrier concentration due to the accumulation of  $\text{Sm}^{3+}$  ions inside the BT phase causes an increase in dielectric loss. The huge improvement in the various ferroelectric parameters is related to domain pinning, oxygen vacancies, and lattice distortion. The saturation and remnant magnetization decline is due to a mismatch of ionic radii and magnetic moments of  $\text{Sm}^{3+}$ ,  $\text{Fe}^{3+}$ , and  $\text{Ba}^{2+}$  ions. The obtained findings can be useful to enhance the performances of magneto-dielectric composite-based multifunctional systems.

**Acknowledgements** The authors thank MANF funds through the UGC fellowship Program under the project F1-17.1/2016-17/MANF-2015-17-MAD-55974/(SA-III/website). The author thanks UGC DAE CSR, Indore for providing most of the experimental facilities for sample characterization like XRD, ferroelectric, and dielectric and also thanks Dr. Sujay Chakravarty of UGC-DAE-CSR, Kalpakkam, India for providing the VSM facility.

**Author contributions** Conceptualization: MK, JS; methodology: AM & PS; formal analysis and investigation: MK, JS; writing—review and editing: MK & PS.

**Funding** The work was supported by Maulana Azad National Fellowship with reference no given. The fellow was Mehjabeen Khan.

## Declarations

**Conflict of interest** The authors declare that they have no conflict of interest.

## References

1. Y. Wang, J. Hu, Y. Lin, C.W. Nan, *NPG Asia Mater.* **2**, 61 (2010)
2. N. Kumar, A. Shukla, R.N.P. Choudhary, *J. Alloys Compd.* **747**, 895 (2018)
3. L. Thansanga, A. Shukla, N. Kumar, R.N.P. Choudhary, *Mater. Chem. Phys.* **263**, 124359 (2021)
4. N. Kumar, A. Shukla, N. Kumar, R.N.P. Choudhary, A. Kumar, *RSC Adv.* **8**, 36939 (2018)
5. M. Khan, A. Mishra, J. Shukla, S. Bisen, P. Sharma, in *AIP Conf. Proc.* (2019)
6. N. Kumar, A. Shukla, N. Kumar, R. Agarwal, R.N.P. Choudhary, *Ceram. Int.* **47**, 22147–22154 (2021)
7. H. Palneedi, V. Annapureddy, S. Priya, J. Ryu, *Actuators* **5**, (2016)
8. V. Kuldeep, O. Subohi, and R. Kurchania, *Appl. Phys. A* **1** (2019)
9. R. Grigalaitis, M.M. Vijatovi, J.D. Bobi, A. Dzunuzovic, R. Sobiestianskas **40**, 6165 (2014)
10. A.S. Dzunuzovic, M.M. Vijatovic Petrovic, J.D. Bobic, N.I. Ilic, M. Ivanov, R. Grigalaitis, J. Banys, B.D. Stojanovic, *Ceram. Int.* **44**, 683 (2018)
11. K. Chand, R.K. Kotnala, *Mater. Chem. Phys.* **174**, 120 (2016)
12. R.S. Devan, Y.R. Ma, B.K. Chougule, *Mater. Chem. Phys.* **115**, 263 (2009)
13. S.N. Babu, K. Srinivas, T. Bhimasankaram, *J. Magn. Magn. Mater.* **321**, 3764 (2009)
14. B.K. Bammannavar, L.R. Naik, *J. Magn. Magn. Mater.* **321**, 382 (2009)
15. R. D. Shannon, *Acta Crystallogr. Sect. A* (1976)
16. M. Khan, S. Bisen, J. Shukla, A. Mishra, and P. Sharma, *J. Supercond. Nov. Magn.* (2020)
17. B. Sarkar, B. Dalal, V. Dev Ashok, K. Chakrabarti, A. Mitra, S.K. De, *J. Appl. Phys.* **115**, 123908 (2014)
18. R. Samad, M.D. Rather, B. Want, *J. Alloys Compd.* **715**, 43 (2017)
19. M. Khan, A. Mishra, J. Shukla, and P. Sharma, in *AIP Conf. Proc.* (2019)
20. M. Khan, A. Mishra, J. Shukla, S. Bisen, P. Sharma, *AIP Conf. Proc.* **2115**, 1 (2019)
21. M. Khan, A. Mishra, J. Shukla, P. Sharma, *AIP Conf. Proc.* **2142**, (2019).
22. J. Shukla, S. Bisen, M. Khan, A. Mishra, *AIP Conf. Proc.* **2115**, (2019).
23. D. Han, D. Lu, F. Meng, *RSC Adv.* **9**, 4469 (2019)
24. H. Sun, X. Wang, X. Yao, *Ferroelectrics* **404**, 99 (2010)
25. A. Kumari, K. Kumari, F. Ahmed, A. Alshoaibi, P.A. Alvi, S. Dalela, M.M. Ahmad, R.N. Aljawfi, P. Dua, A. Vij, S. Kumar, *Vacuum* **184**, 109872 (2021)
26. H. Kumar, J.P. Singh, R.C. Srivastava, P. Negi, H.M. Agrawal, K. Asokan, *J. Nanosci.* **2014**, 1 (2014)
27. A. Manzoor, M.A. Khan, M.Y. Khan, M.N. Akhtar, A. Hussain, *Ceram. Int.* **44**, 6321 (2018)
28. A. Abdel Aal, T.R. Hammad, M. Zawrah, I.K. Battisha, A.B. Abou Hammad, *Acta Phys. Pol. A* **126**, 1318 (2014)
29. G.R. Gajula, L.R. Buddiga, K.N. ChidambaraKumar, N. Vattikunta, M. Dasari, *Phys. B Condens. Matter* **560**, 1 (2019)
30. B. Ni, Z. Fe, R. Zhang, C. Deng, L. Ren, Z. Li, J. Zhou, *Mater. Res. Bull.* **48**, 4100 (2013)
31. S. Magnet, K. Barium, *F. Magnes.* **46**, 967 (2017)
32. H. Yang, H. Wang, L. He, X. Yao, *Mater. Chem. Phys.* **134**, 777 (2012)
33. A. Radoń, Ł. Hawełek, D. Łukowiec, J. Kubacki, P. Włodarczyk, *Sci. Rep.* **9**, 1 (2019)
34. M. Khan, S. Bisen, J. Shukla, A. Mishra, P. Sharma, *J. Supercond. Novel Magn.* **34**, 763–780 (2020)
35. F. Giannici, G. Gregori, C. Aliotta, A. Longo, J. Maier, A. Martorana, *Chem. Mater.* **26**, 5994 (2014)

36. R.P. Mahajan, K.K. Patankar, M.B. Kothale, S.C. Chaudhari, V.L. Mathe, S.A. Patil, *Pramana* **58**, 2 (2002)
37. A. Sinha, A. Dutta, *J. Phys. Chem. Solids* **145**, 109534 (2020)
38. A. K. Jonscher, *Dielectric relaxation in solids* **57** (1999)
39. S. Bisen, M. Khan, A. Mishra, *J. Mater. Sci. Mater. Electron.* **31**, 9212 (2020)
40. S.K. Upadhyay, V.R. Reddy, N. Lakshmi, *Integr. Med. Res.* **1**, 346 (2018)
41. S.M. Mane, A.R. Nimbalkar, H. Kim, S.B. Kulkarni, N.T. Tayade, J.V. Thombare, S.S. Dhasade, J.C. Shin, *J. Alloys Compd.* **849**, 156599 (2020)
42. A. R. Makhdoom, M. J. Akhtar, M. A. Rafiq, M. M. Hassan, *Ceram. Int.* (2012)
43. M. T. Rahman, C. V. Ramana, *J. Appl. Phys.* (2014)
44. M. Shariq, D. Kaur, V. Singh, C. Praveen, K.J. Sasi, M. Sharma, S. Hussain, *Arab. J. Sci. Eng.* **44**, 613 (2019)

**Publisher's Note** Springer Nature remains neutral with regard to jurisdictional claims in published maps and institutional affiliations.

Springer Nature or its licensor (e.g. a society or other partner) holds exclusive rights to this article under a publishing agreement with the author(s) or other rightsholder(s); author self-archiving of the accepted manuscript version of this article is solely governed by the terms of such publishing agreement and applicable law.